IEEE Access
Multidisciplinary ⋮ Rapid Review ⋮ Open Access Journal

Received 4 July 2024, accepted 19 July 2024, date of publication 29 July 2024, date of current version 7 August 2024.

Digital Object Identifier 10.1109/ACCESS.2024.3435467

RESEARCH ARTICLE

Development and Application of a Novel High Precision Six-Axis Force/Torque Sensor

WEIZHENG REN[1], KAILE YU[1,2], YIRAN ZHANG[2], YUTONG GE[2], AND YUXIAO LI[2]
[1]School of Modern Post, Beijing University of Posts and Telecommunications, Beijing 100876, China
[2]School of Electronic Engineering, Beijing University of Posts and Telecommunications, Beijing 100876, China

Corresponding author: Weizheng Ren (Renwz_lw@163.com)

ABSTRACT Improving the accuracy of the six-axis force sensor Six-axis force sensors (hereafter collectively referred to as 6a-sensors) is a systematic problem, which mainly involves the optimization and improvement of three aspects: the design of the elastic body of the 6a-sensors, the acquisition and processing of the weak signal, and the decoupling of the inter-dimensional data of the force and torque of each dimension. To attain high stiffness, sensitivity, and minimal coupling, a design scheme of cross beam elastomer based on titanium alloy material is proposed. In order to realize the acquisition and processing of multi-channel weak differential signals with high gain, high linearity and precision, a high-speed programmable weak signal processing circuit design scheme is proposed. To efficiently address the interdependence issue among signal dimensions in the 6a-sensors. This paper innovatively proposes a BP-PSO decoupling algorithm using Particle Swarm Approach (PSO) to optimise the optimiser of BP neural network. To validate the algorithm's effectiveness, comparative experiments are conducted with the 6a-sensors. designed and studied in this paper by sampling and self-designed calibration system. The sensitivity of the 6a-sensor designed in this paper reaches 4mV/V. In terms of accuracy, there is an improvement of about 1%. In terms of crosstalk, there is an improvement of about 0.2%. providing a new and improved idea for the six-dimensional force decoupling algorithm. In order to further verify the practicability of the algorithm, a flexible surface grinding robot based on six-axis force is developed based on Siasun robot platform. The grinding strength control is accurate, and the running trajectory is uniform and smooth, which can effectively meet the practical application requirements of flexible and intelligent control.

INDEX TERMS Data decoupling, elastomer design, flexible grinding, weak signal processing, 6a-sensors.

I. INTRODUCTION

A. RESEARCH BACKGROUND

With the increasingly complex working conditions and working modes of equipment and the increasingly prominent demand for intelligence, modern industrial equipment has increasingly high requirements for force sensing and control. The contact process almost runs through all links of modern processing and manufacturing. Accurate and fast measurement of force and torque represented by ''contact load'' is an important guarantee for realizing intelligent processing and manufacturing [1]. It is one of the key technical challenges for smart devices and robots to realize compliant and intelligent operation [2]. On the basis of taking into account the size requirements, it is necessary to accurately and quickly sense the three-dimensional space force and three-dimensional space torque, and realize feedback control. Hence, there is a pressing requirement to design a high-performance integrated 6a-sensors, encompassing both three-axis force and three-axis torque measurements. However, in the practical process of developing a 6a-sensors, enhancing its accuracy emerges as a comprehensive challenge. The static measurement model of the statically indeterminate 6a-sensors is established, which lays a theoretical and experimental foundation for the calibration research of the statically indeterminate 6a-sensors. In order to effectively improve the measurement accuracy of the 6a-sensors, it is necessary to systematically solve the problem of the elastic body structure

The associate editor coordinating the review of this manuscript and approving it for publication was Chun-Wei Tsai.

design of the 6a-sensors, the problem of weak signal acquisition and processing, and the problem of inter-dimensional data decoupling of forces and torques of each dimension. To this end, this paper will systematically put forward a new high-precision six-axis force design scheme, and conduct in-depth research on the main key technologies designed to improve the measurement accuracy of the 6a-sensors and put forward innovative solutions. Using a low-coupling cross beam structure design, high precision and high speed weak signal processing circuit design and inter-dimensional decoupling algorithm based on particle swarm BP neural network, a compact titanium alloy resistance strain type 6a-sensors is designed and developed. In order to further verify the practicability of the algorithm, a calligraphy robot based on six-axis force is developed based on Siasun robot platform. The writing strength control is accurate, and the handwriting is uniform and smooth, which can effectively meet the practical application requirements of compliant and intelligent control. It presents a novel idea for the evolution of a multi-dimensional force sensor for accurate and fast measurement of load in the process of surface grinding, heterosexual welding, medical rehabilitation and other flexible and intelligent operation.

B. LITERATURE REVIEW

The earliest study of 6a-sensors can be traced back to the 1970s, and the United States, Japan and other countries have carried out the study of 6a-sensors. The application significance of the 6a-sensors extends to specialized domains including precision assembly, contour tracking two-handed coordination control [3], automotive wheel force testing, aircraft landing force detection, rocket thrust measurement, transient space station docking, and real-time acquisition of the center of gravity data for ejection seat systems [4]. Six-dimensional force sensors are also widely used in robotic work, and the force and torque data collected by the sensors form the basis of force-controlled feedback in robots. Fu and Song proposed a new 6a-sensors based on polyetheretherketone (PEEK) material. By establishing a simplified static mathematical model, compared with the ordinary 6a-sensors, the 6a-sensors made of PEEK material has higher sensitivity, but the established mathematical model cannot achieve accurate prediction of sensor performance [5].

The theoretical mathematical model of the sensor still needs to be further studied [6]. Yan et al. based on the design method of the full-shear 6a-sensors with symmetrical integral structure for strain measurement, used finite element analysis to carry out static and dynamic analysis of the elastic body, realized the optimal design of the elastic body structure size and the determination of the patch position, and obtained good performance indicator [7]. In order to improve the dynamic performance of the existing 6a-sensors, Li and Zhang proposed a new elastomer structure of the 6a-sensors, which has good dynamic performance and promotes the development of multi-dimensional force sensors for high-speed robots. The structure of the elastic 6a-sensors is complex, and the development of the inelastic 6a-sensors can further improve the dynamic performance [8]. Wang and Yao obtained the full mapping relationship between the generalized external force including the action of the intermediate preloaded branch and the axial forces of the six measured branches for a 6a-sensors with preloaded statically overdetermined Stewart structure, by comprehensively considering the displacement coordination relationship between the overall stiffness of the sensor and the deformation of the branch rod [9]. The static measurement model for the statically indeterminate 6a-sensors is formulated, providing a theoretical and experimental basis for the calibration investigation of the statically indeterminate 6a-sensors. However, the precise theoretical mathematical model of the 6a-sensors based on Stewart structure is not established, and the dynamic characteristics of the 6a-sensors cannot be predicted. Niu et al. designed a set of micro-sensor signal acquisition system based on FPGA [10], and Liu et al. designed a set of force sensor signal acquisition and processing system based on STM32, which solved the processing and analysis of sensor signals from the perspective of hardware [11]. Wang et al. developed a six-dimensional force sensor with a circular flexible connection, which gave a new research perspective in terms of stiffness analysis and parameter optimisation, respectively [12]. Ha and Kang provided an economical and friendly wireless communication solution for six-dimensional force sensors, which gave another new way of connectivity and production [13]. Kebede and Ahmad proposed a 6a-sensors based on strain gauge structure, which adopted the least square method and error reduction technology to realize the calibration of robust decoupling matrix and improve the sensitivity of decoupled 6a-sensors [14]. The 6a-sensors based on elastic body strain type has complex decoupling and is easy to introduce coupling errors. Chavez and Traversaro studied the dynamic performance calibration method of the 6a-sensors used by floating robots and its influence [15]. The field calibration method based on mathematical model has shown good effect in improving the measurement of the 6a-sensors. The mathematical model is relatively simple, and the test method is complex, so it is impossible to predict the dynamic characteristics of the sensor before the test [16].

In this paper, a decoupling algorithm based on PSO-BP neural network algorithm is proposed, which uses PSO algorithm to optimize the optimizer in the neural network and provides a new idea for decoupling algorithm.

II. DESIGN OF SYSTEM ARCHITECTURE

The 6a-sensors primarily consists of three components: stress sensing unit, signal processing unit and data processing unit.

The stress sensing unit mainly includes two parts: the sensor elastic body and the strain measurement bridge. The strain gauge of the strain bridge is pasting in the strain area of the elastic body. When the elastic body is subjected to external force, the strain area will be deformed, which will lead to the deformation of the strain gauge, so that the resistance of each

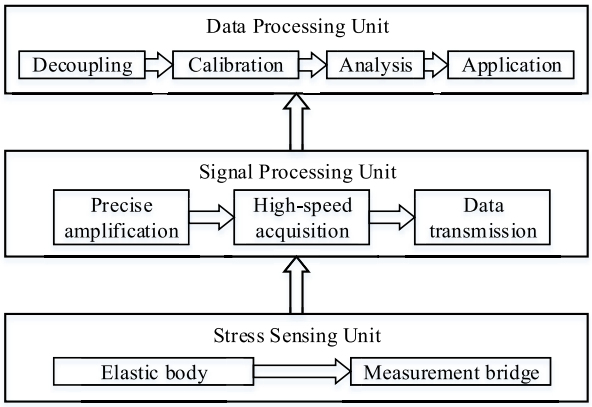

FIGURE 1. Six-dimensional force /torque sensor system block diagram.

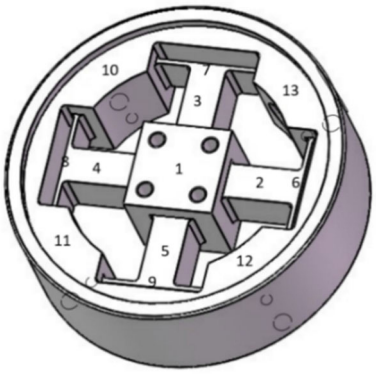

1: Central platform, 2-5: Main beam, 6-9: Floating beam, 10-13: Flange

FIGURE 2. The elastic beam structure of small six-dimensional force /torque sensor.

arm of the measurement bridge changes, and the differential measurement signal is generated.

The signal processing unit includes three modules: precise amplification, high-speed acquisition and data transmission. The precision amplifier module is responsible for amplifying the differential measurement signal input of the stress sensing unit to 0.5 V-4.5 V, which provides a standard voltage signal for the subsequent AD acquisition. The high-speed acquisition module is in charge of sampling and converting the voltage signal ranging from 0.5 V to 4.5 V, which is supplied by the precision amplifier module, into a digital signal.

The data transmission module is tasked with transferring the AD-sampled data to the data processing unit of the host computer through various transmission modes.

The data processing unit is responsible for decoupling, calibration, analysis and application of the data transferred from the lower computer. The specific functions will be described in detail in Chapter VI (see Figure 1).

III. DESIGN OF STRESS SENSING UNIT

A. DESIGN AND ANALYSIS OF SENSOR ELASTOMER

In the process of designing the sensor, the design of the sensitive element, i.e., elastomer, is particularly important, and its design directly affects the accuracy of the sensor. Numerical analysis is used to calculate the distribution of stress and strain in the elastomeric material. in the loading and unloading process, in order to verify the reasonableness of its structural design, and to determine the size that meets the requirements, as well as the positioning for affixing the strain gauges.

1) ELASTOMER STRUCTUREOR

To achieve the sensor with small coupling and a compact structure, the designed 6a-sensors in this paper utilizes a unified spoke-type crossbeam structure. It is anchored and supported by four center-symmetric rims. The crossbeam is segmented into four square prismatic main beams, each connected to the rims through a floating beam. Resistive strain gauges are pasted around the four main beams to form a strain bridge to sense the three-axis forces Fx, Fy, Fz and three-axis torques Mx, My, Mz in the three-dimensional space, and the force axis transmits the force to the elastomer through the threaded fit with the central platform, and this structure has the advantages of mutual decoupling of the dimensions, no radial effect, and easy calibration [17]. The structure is shown in Figure 2, and the sensitive force/torque coordinate system is a right-handed coordinate system.

TABLE 1. Elastic beam dimension parameter.

	cross beam	floating beam	central platform	flange	flange hole
length	15	22	20		
width	8	1	20		
height	8	8	24	24	24
diameter				50/68	3.2

2) FINITE ELEMENT ANALYSIS OF ELASTOMER

Upon establishing the elastomer's structure, a finite element analysis is conducted using ABAQUS software. The dimensional parameters of the elastomer first need to be determined in terms of the approximate volume, i.e., the outer rim diameter and thickness, based on the environment in which it will be used. Under the condition of volume determination, the range and sensitivity of the resistance strain gauge six-dimensional force sensor are contradictory, which are primarily influenced by the floating beam and main beam's thickness and length. Therefore, it is necessary to consider the volume, sensitivity, overload capacity and other factors to obtain the optimal elastomer size parameters through continuous adjustment.

As shown in Table 1, the finalized detailed size parameters of the elastomer, the sensor fabricated in this paper and the corresponding analysis results are based on this size. The sensor's elastomer is crafted from durable, fatigue-resistant 2A12-T4 hard aluminum alloy, featuring an elasticity modulus E of 73.4×10^9 Pa and a Poisson's ratio $\mu = 0.33$.

SOLIDWORKS2019 was used to establish the elastomer model, and ABAQUS2021 was imported for finite element selection and mesh division. C3D10 high-precision solid

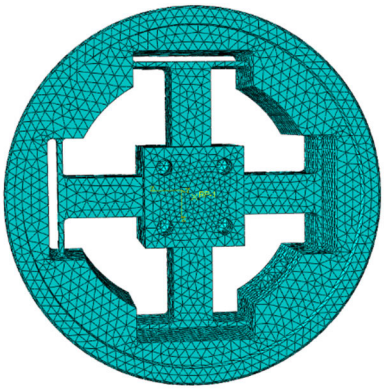

FIGURE 3. Elastomer finite element model.

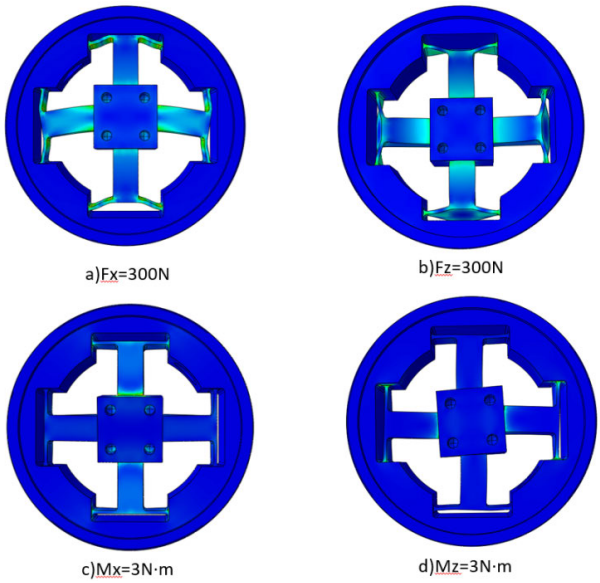

FIGURE 4. Elastic beam strain diagram after loading.

element was selected, and the generated finite element model was shown in Figure 3.

After the elastomer finite element model is established, it needs to be loaded and solved to analyze the strain after the force is applied. Firstly, the constraints of the elastomer are set. Since the elastomer is fixed to the base through four screw holes on the rim, the XYZ degrees of freedom of the four screw holes are set to zero.

Due to the symmetry of the sensor, the strain of the force and torque in the X and Y directions are similar, so only four directions, Fx, Fz, Mx, and Mz, require loading and analysis, and the loading values are based on design specifications. In the context of the design application of this paper, the measurement range of the sensor is Fx,y,z = ±300N, Mx,y,z = ±3N·m, and the overload capacity is Fx,y,z = ±500N, Fx,y,z = ±5N·m. The results can be obtained by solving separately for each dimension of loading as shown in Figure 4.

To accurately determine the placement of the resistive strain gauges, it is necessary to analyze the correspondence between the strain on the main beam and the distance from

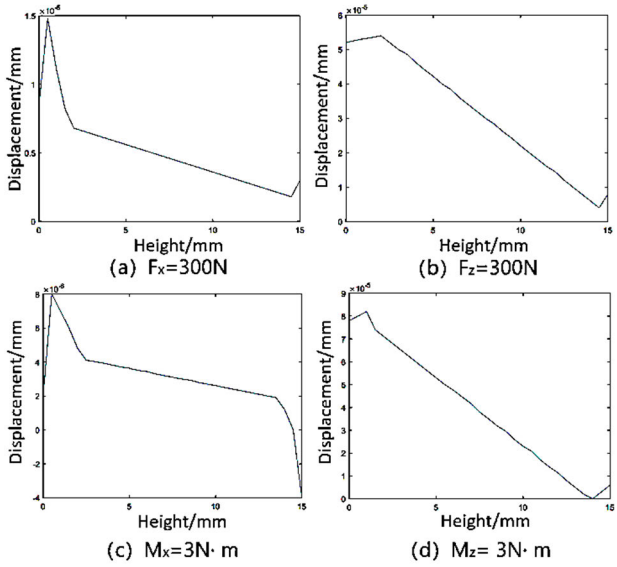

FIGURE 5. Path mapping strain diagram.

the central platform. Employing the path mapping feature in ANSYS software, a path is defined from the platform to the floating beam on the main beam's surface. The strain in the main beam during force/moment is then mapped to this path. The loading in each dimension is solved separately and the results are depicted in Figure 5, where the horizontal axis indicates the distance from the center of the camber and the vertical axis indicates the magnitude of the strain at each location on that path.

In order to ensure that the stress sustained by the elastic beam in the limit case of applied multi-axis force is within the permissible stress range of the material, it is necessary to load the elastic beam with full scale force or torque in six directions simultaneously, and the strain of the elastic beam is shown in Figure 6.

The maximum strain on all paths is 1.752×10^{-3}, $\varepsilon \times E = (1.752 \times 10^{-3}) \times 73.4\text{GPa} \approx 106.65\text{MPa}$, which is smaller than the yield strength of 2A12-T14 hard aluminum alloy of 325MPa, which indicates that the structure complies with the strength design specifications.

According to the results of Figure 5 can determine the patch position of the resistance strain gage, in the interval of 4 to 13 mm from the central platform, the distance from the platform and the size of the strain is a linear relationship, close to the central platform at the maximum strain. To maximize sensor sensitivity, strain gauges for measuring force values are adhered approximately 4mm from the center tab, and the strain gauges for measuring the moment value are pasted at 9mm from the central platform.

B. DESIGN OF HIGH-SPEED ACQUISITION CIRCUIT

The measurement bridge of the 6a-sensors adopts a full-bridge resistance strain type four-arm measuring bridge, with each force/torque direction corresponding to a four-equal-arm full-bridge circuit. In light of the analysis of the

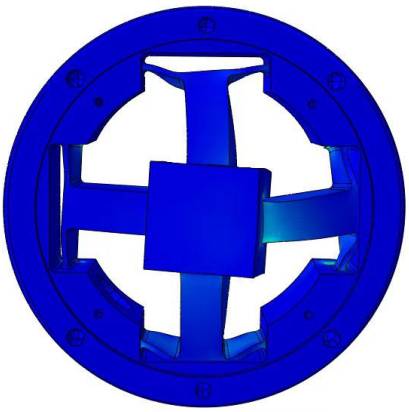

FIGURE 6. Elastic beam strain diagram under extreme condition.

position of strain gauge patch, the final position of strain gauge patch is shown in Figure 7. The bridge circuit, as illustrated in Figure 8, employs VR as the reference voltage for optimal sensitivity in the 6a-sensors. Despite a 5V power supply, a stable 24V reference voltage is ensured for VR using a boosting circuit. The output signals include VX for force in the X direction, VY for force in the Y direction, VZ for force in the Z direction, VMX for torque in the X direction, VMY for torque in the Y direction, and VMZ for torque in the Z direction.

IV. DESIGN OF SIGNAL PROCESSING UNIT

A. DESIGN OF PRECISION AMPLIFIER CIRCUIT

The value of each differential voltage signal obtained by metal strain gauge conversion is millivolt level. In order to improve the sensitivity of the sensor, considering the performance index of the subsequent A/D conversion circuit, the differential voltage signal is amplified to 0.5V-4.5V by the amplifier circuit. Based on the theoretical full-scale bridge output calculated in Section A, Chapter III, it can be seen that the theoretical magnification of the six-way amplifier circuit is 610 times in the Fx(Fy) direction, 438 times in the Fz direction, 1 451 times in the Mx(My) direction, and 1 143 times in the Mz direction. Because of the large amplification ratio of the system, the signal distortion will be obvious if only single stage amplification is used, so the signal conditioning chip JHM1101 nested DC booster amplifier circuit is used to precisely amplify the millivolt level differential signal of the strain bridge. Considering the nonlinear and temperature drift problems between the differential signal output of strain bridge and the actual stress, a signal conditioning chip JHM1101 designed for Wheatstone bridge sensor is used in the first stage amplifier circuit. The sensor nonlinear correction algorithm of JHM1101 can correct and compensate the nonlinear and temperature drift characteristics of the sensor in the first or second order, so as to output the measurement results of high linearity. When the Wheatstone bridge needs temperature compensation, the JHM1101 also provides an integrated high linear temperature Sensor (Temp Sensor), the user can also choose to use the off-chip diode to measure the

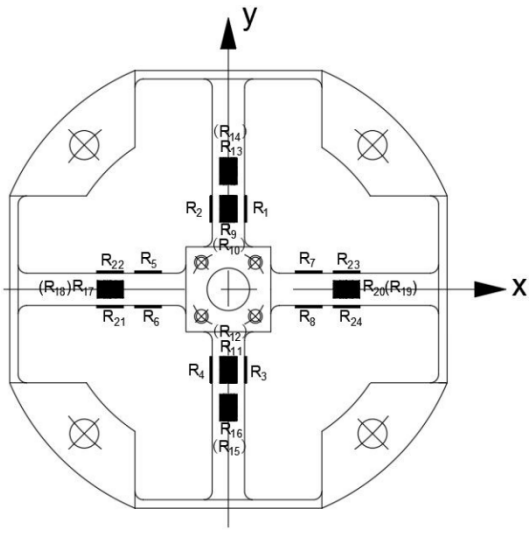

FIGURE 7. Elastic beam SMD and bridge structure diagram.

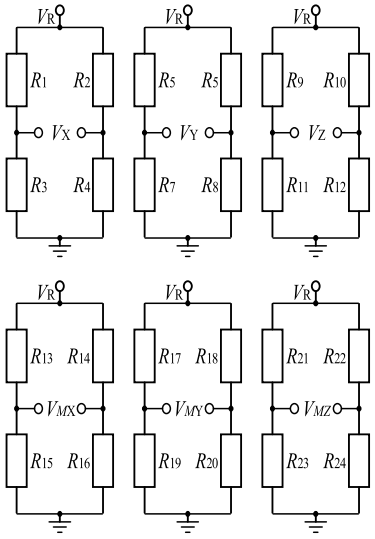

FIGURE 8. Bridge circuit diagram.

temperature of the sensor location. In addition, the output value of the force and torque measurement bridge in each direction is quite different

Through the programmable conditioning function of JHM1101, no matter how much the output value of the bridge in each direction is, the standard voltage output of 0.5V-4.5V can be amplified through JHM1101, which brings convenience to the subsequent amplifier circuit design and data acquisition circuit design.

In order to enhance the sensitivity of the sensor, without changing the structure of the elastomer and the power supply voltage, the SX1308 boost regulator circuit is used to boost the reference voltage provided by the JHM1101, and the stabilized voltage after boosting is provided to the strain bridge as the reference voltage of the bridge to enhance the magnitude of the differential signal output from the bridge, which in turn enhances the sampling sensitivity of the sensor. The reference voltage provided on the JHM1101 chip is 5V,

and it is boosted to 24V by SX1308, which correspondingly increases the differential signal output of the bridge by about 5 times, thus achieving a five-fold increase in the sampling sensitivity of the sensor.

B. DESIGN OF HIGH-SPEED ACQUISITION CIRCUIT

In order to meet the requirements of high-speed dynamic performance of 6a-sensors, this system does not use the AD conversion function of STM32F103C8T6 processor, but uses high-speed and high-resolution AD7606. The AD7606, a 16-bit, 6-channel synchronous sampling AD chip from Analog Devices (ADI), offers a parallel sampling rate of up to 200KSPS. It features integrated analog input clamp protection, a second-order anti-alias filter, track and hold amplifier, and a 16-bit charge redistribution successive approximation ADC core. The chip supports high-speed serial and parallel interfaces. Operating on a single 5V power supply, the AD7606 eliminates the need for a positive and negative dual power supply. It accommodates $\pm$10V or $\pm$5V bipolar signal inputs. All channels can be sampled at rates up to 200KSPS, and the input clamping protection circuitry can withstand voltages up to $\pm$16.5V. By enabling synchronous sampling of six channels at a single rate of 200KSPS with 16-bit resolution, the AD7606 significantly enhances the sensitivity and accuracy of the 6a-sensors.

C. CONFIGURABLE DATA TRANSMISSION MODES

In order to meet the use of different scenarios, the system adopts configurable data transmission modes, mainly including RS-422 serial communication, Ethernet network communication and LoRa wireless communication three data transmission modes.

The default connection is RS-422 serial port, and the sensor communication is carried out with a special multi-core cable. the RS-422 four-wire interface does not have to control the data direction because it uses separate transmit and receive channels, and the maximum transmission rate is 10Mb/s, which is very suitable for the high-speed transmission rate requirements of the six-axis force.

Due to the popularity of the industrial Internet, 6a-sensorss must also be adapted to the needs of the network environment, for this system designed the Ethernet communication mode, Ethernet communication port can be connected to both PCs used for development and robots can be connected to collaborative work. At the same time, it also provides convenience for remote control in the industrial Internet environment.

In order to meet the different application scenarios of six-axis forces, wireless data transmission is also a necessary configuration. This system uses Ra-06 LoRa module to design the wireless data transmission function. Ra-06 LoRa is based on Semtech SX1276/SX1278 LoRa spread spectrum modulation technology, with ultra-high receiving sensitivity, strong anti-interference ability. Using efficient forward error correction coding technology, with a very low bit error rate, and long-term stable data transmission capability.

V. RESEARCH ON DECOUPLING ALGORITHM

In an ideal 6a-sensors, the voltage value of the output channel in each direction depends only on the force/torque in that direction, and is nothing to do with the force/torque acting in the remaining five directions. However, due to the structural design of the sensor, patch technology, strain gauge transverse effect, etc., it is inevitable that the force/torque components acting on the sensor in each dimension will have an effect on the output signals of the sensor in each direction, generating inter-dimensional coupling and thus affecting the accuracy of the sensor. To address this problem, this paper proposes a decoupling algorithm based on BP neural network, which is characterized by strong operability, fast decoupling operation speed, good nonlinear mapping ability [18], etc., so that the sensor has a wide range of applicability, strong sensing sensitivity and high detection accuracy.

A. DESCRIPTION OF DECOUPLING PROBLEM

In order to describe more clearly the correspondence between the force/torque exerted by the six directions of the 6a-sensors and the voltage signals output from the sensor in the corresponding directions, it is assumed that is the force/torque exerted by the six directions of the 6a-sensors. The measured voltage vector is $U = \left(U_{F_x}, U_{F_y}, U_{F_z}, U_{M_x}, U_{M_y}, U_{M_z}\right)^T$, which represents the six voltage signals generated by the sensor under the force/torque applied in six dimensions.

Set the coefficient matrix

$$K = \begin{bmatrix} k_{11} & k_{12} & k_{13} & k_{14} & k_{15} & k_{16} \\ k_{21} & k_{22} & k_{23} & k_{24} & k_{25} & k_{26} \\ k_{31} & k_{32} & k_{33} & k_{34} & k_{35} & k_{36} \\ k_{41} & k_{42} & k_{43} & k_{44} & k_{45} & k_{46} \\ k_{51} & k_{52} & k_{53} & k_{54} & k_{55} & k_{56} \\ k_{61} & k_{62} & k_{63} & k_{64} & k_{65} & k_{66} \end{bmatrix} \tag{1}$$

making

$$F = KU \tag{2}$$

i.e.

$$\begin{bmatrix} F_x \\ F_y \\ F_z \\ M_x \\ M_y \\ M_z \end{bmatrix} = \begin{bmatrix} k_{11} & k_{12} & k_{13} & k_{14} & k_{15} & k_{16} \\ k_{21} & k_{22} & k_{23} & k_{24} & k_{25} & k_{26} \\ k_{31} & k_{32} & k_{33} & k_{34} & k_{35} & k_{36} \\ k_{41} & k_{42} & k_{43} & k_{44} & k_{45} & k_{46} \\ k_{51} & k_{52} & k_{53} & k_{54} & k_{55} & k_{56} \\ k_{61} & k_{62} & k_{63} & k_{64} & k_{65} & k_{66} \end{bmatrix} \begin{bmatrix} U_{F_x} \\ U_{F_y} \\ U_{F_z} \\ U_{M_x} \\ U_{M_y} \\ U_{M_z} \end{bmatrix} \tag{3}$$

then we have

$$K = FU^T \tag{4}$$

The 6a-sensors in the ideal state, the signals of each circuit do not have inter-dimensional coupling, then we have

$$\begin{bmatrix} F_x \\ F_y \\ F_z \\ M_x \\ M_y \\ M_z \end{bmatrix} = \begin{bmatrix} k_{11} & 0 & 0 & 0 & 0 & 0 \\ 0 & k_{22} & 0 & 0 & 0 & 0 \\ 0 & 0 & k_{33} & 0 & 0 & 0 \\ 0 & 0 & 0 & k_{44} & 0 & 0 \\ 0 & 0 & 0 & 0 & k_{55} & 0 \\ 0 & 0 & 0 & 0 & 0 & k_{66} \end{bmatrix} \begin{bmatrix} U_{F_x} \\ U_{F_y} \\ U_{F_z} \\ U_{M_x} \\ U_{M_y} \\ U_{M_z} \end{bmatrix} \tag{5}$$

The 6a-sensors in reality, due to the 6a-sensors structure design and other reasons, it is impossible to avoid that the signals collected by each road are affected by the other roads, resulting in the phenomenon of inter-dimensional coupling. In recent years, many scholars have made a more in-depth study on the decoupling algorithm of multidimensional force sensors, in which the static decoupling based on linear calibration and based on least-squares linear fitting can only reduce the inter-dimensional coupling by one order of magnitude, and the decoupling result still exists with a coupling error of 0.2% $\sim$ 0.5%, which is not up to the requirement of its accuracy in the process of precision manufacturing [19]. Mao et al. proposed a decoupling algorithm based on one-dimensional linear coupling error modeling, the decoupling accuracy is high, but if based on the multistep coupling error, its arithmetic is large, and is not suitable for application in practice [20]. Jiang et al. proposed a decoupling method based on artificial BP neural network, and decoupling experimental simulation of the five-axis fingertip force/torque sensors [21], and the results show that this algorithm has a good effect and high accuracy of the decoupling. The algorithm is applied to the decoupling study of the developed 6a-sensors with resistance strain gauges, and some problems are found during the training process of the neural network, especially the phenomena of local minima and slow convergence, which may result in decoupling failure. Therefore, an algorithm based on improved BP neural network is proposed. The algorithm retains the advantages of BP neural network decoupling, and improves the traditional BP neural network by utilizing PSO's global optimization, which solves the problems of oscillation, slow convergence, and local minima that occur during the training process [22]. In addition, Wang et al. proposed a polynomial-based decoupling from the decoupling principle, which can effectively improve the decoupling speed, but the decoupling accuracy is still insufficient [23]. The experimental decoupling shows that the improved particle swarm optimization BP neural network algorithm is easy to implement in the decoupling process of the six-dimensional force sensor, fast convergence speed, good decoupling effect, and has a good engineering application prospect in decoupling control.

B. MODELING OF DECOUPLING ALGORITHM

Inter-dimensional decoupling involves establishing a transfer relationship between the measured voltage and the desired voltage in each stress dimension. The use of an improved BP neural network eliminates the need for predicting mathematical equations, as it can learn and characterize the nonlinear mapping relationship between inputs and outputs. The BP neural network, employing a gradient descent learning rule, adjusts weights and thresholds through directional propagation correction, minimizing the sum of squared errors. By employing the BP neural network to simulate the mapping relationship in the K matrix, and applying this approach to inter-dimensional decoupling for a 6a-sensors, it effectively mitigates intrinsic inter-dimensional coupling caused by elastomer structural factors, thereby enhancing measurement accuracy.

The BP neural network structure designed for six-axis force data decoupling is depicted in Figure 9, comprising one input layer, three hidden layers, and one output layer. Reflecting the inherent characteristics of the 6a-sensors, the decoupling model transforms the six-axis strain output voltage into decoupled output voltage. The input layer receives the six-axis measurement feature vector, while the output layer processes the six-axis feature vector. Consequently, both layers consist of six neurons each, corresponding to the six-axis feature vectors. Following numerous six-axis force decoupling experiments, it has been determined that the hidden layer adopts a three-layer structure with 36, 36, and 18 neurons in each layer, respectively. $u = [u_1, u_2, u_3, u_4, u_5, u_6]^T$ is the input vector of the network, i.e., the voltage value corresponding to the stress before the decoupling. ω_{ij} is the weight value between the ith unit of the input layer and the jth unit of the hidden layer, ω_{jk} is the weight value between the jth unit of the hidden layer and the kth unit of the output layer. The weights between each layer are similar and will not be repeated here.

In the forward propagation process, $\sigma_1(x)$ is the implicit layer activation function, and after comparing the commonly used activation functions Sigmoid, Tanh, ReLU, etc. through experiments, it is determined that the ReLU function is the implicit layer activation function, i.e., $\sigma_1(x) = \max(0, x)$.$\sigma_2(x)$ is the output layer activation function, and no processing is needed for the implicit to the output layer. The Pureline function is selected as the output layer activation function, i.e., $\sigma_2(x) = x$. $v = [v_1, v_2, v_3, v_4, v_5, v_6]^T$ is the output vector of the network, i.e., the value of the stress mapped voltage after decoupling.

In the process of calculating the loss and back propagation, for the commonly used loss functions such as mean square error, cross entropy, log-likelihood loss, etc., but these methods are prone to slow convergence, fall into the local extremes and other problems, PSO has the advantages of global optimization, fast optimization speed and high accuracy, using the improved PSO to optimize the BP, the training can be completed quickly to achieve the required accuracy. Here, the PSO fitness function is used to evaluate the output solution of BP neural network in training [6]. Specifically, the chosen PSO fitness function is the error term between the actual output and the desired output of the neural network.

$$f(u) = \frac{1}{n} \sum_{i=1}^{n} \left(\hat{u}_i - u_i\right)^2 \tag{6}$$

where $\hat{u}_i$ is the desired output of the ith neuron, n is the number of neural network output units, and u_i is the actual output value of the sample.

To address the limitation of the standard particle swarm optimization algorithm, which may not consider the mutual influence between individual particles, this paper employs an

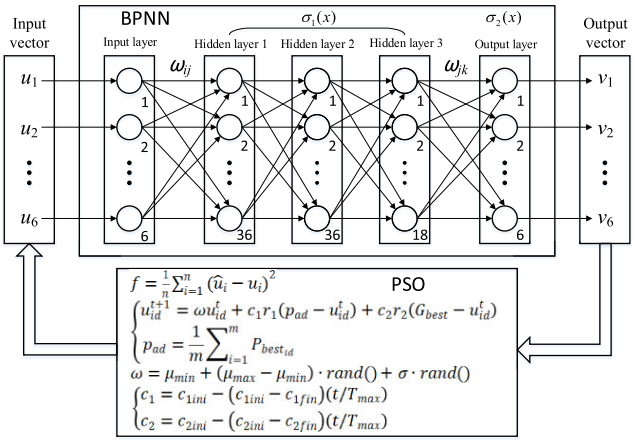

FIGURE 9. Structure diagram of decoupling model of particle swarm BP neural network.

improved particle swarm optimization algorithm as follows.

$$\begin{cases} u_{id}^{t+1} = \omega u_{id}^t + c_1 r_1 \left(p_{ad} - u_{id}^t\right) + c_2 r_2 \left(G_{best} - u_{id}^t\right) \\ p_{ad} = \dfrac{1}{m}\sum_{i=1}^{m} P_{best_{id}} \end{cases} \tag{7}$$

where u_{id}^t is the position of the individual in the tth iteration denotes the position of the individual in the tt-th iteration; ω is the inertia weight; c_1 and c_2 are the factors affecting the individual's "self-cognitive" and "social cognitive" abilities, respectively; r_1 and r_2 are randomized numbers from 0 to 1; G_{best} is the global optimal, and $P_{best_{id}}$ is the individual optimum, and p_{ad} is the average of all individual optimums.

To enhance the global search performance of the algorithm and expedite the escape from local optima, the inertia weight ω is configured as a random number following a specific distribution. This approach is advantageous for fulfilling the demands of refining the search, preventing overshooting the optimal solution space. Moreover, it aligns with the necessities of global particle search, steering clear of local optima and premature convergence, ultimately accelerating the convergence speed of the algorithm. The formula of inertia weight ω is as follows.

$$\omega = \mu_{min} + \left(\mu_{max} - \mu_{min}\right) \cdot rand() + \sigma \cdot rand() \tag{8}$$

where $\mu_{\min}$, $\mu_{\max}$ represent the minimum and maximum values of the mean inertia weights, respectively, rand() is the uniform distribution function, ensuring equal probability of obtaining optimal, maximum, and minimum values within the interval. the influence of the uniform distribution in the weight ω is limited by the $\mu_{\max} - \mu_{\min}$, rand() is the function of normal distribution, and σ is the variance.

Typically, experimental errors follow a normal distribution. In this context, the third term, represented by the normal distribution function σ, is utilized to assess the degree of deviation between the weights ω and their mean value. This term helps control the weighting error, ensuring that the weights evolve in the direction of the mean.

$$\begin{cases} c_1 = c_{1ini} - \left(c_{1ini} - c_{1fin}\right)\left(\dfrac{t}{T_{max}}\right) \\ c_2 = c_{2ini} - \left(c_{2ini} - c_{2fin}\right)\left(\dfrac{t}{T_{max}}\right) \end{cases} \tag{9}$$

where c_{1ini}, c_{2ini} are the initial values of the learning factors c_1, c_2, c_{1fin}, c_{2fin} are the final values of learning factors c_1, c_2; t is the current number of iterations; T_{max} is the maximum number of iterations.

C. PROCESS OF DECOUPLING ALGORITHM

The decoupling model of BP neural network optimized based on particle swarm algorithm can be divided into three major parts: network construction, training and learning, parameter optimization and decoupling output, the specific steps are described below

Step 1: Initialize the BP neural network structure. The number of nodes in the input layer of the neural network and the output layer of the neural network are set according to the actual problem, load the data and carry out normalization preprocessing, set the values of other parameters such as the number of training samples, the number of test samples, the maximum number of training times, the target error, etc.; according to the experimental experience to determine the value of the number of neurons in the implied layer, establish the BP neural network, train and learn the sample data set.

Step 2: Initialize the dimension and size of the particle swarm, randomly initialize the position of each particle within a certain range of values, and set the values of other parameters of the particle swarm algorithm, such as the learning factor, the upper and lower limits of the position values, and the maximum number of iterations.

Step 3: Calculate the fitness value of each particle, set the position of the ith particle as the current optimal position of the particle $P_{best_{id}}$, and compare the fitness values of all $P_{best_{id}}$ $P_{best_{id}}$ to select the optimal position of the particle in the population and store it in G_{best}.

Step 4: Combine (7), (8) and (9) to update the position u_i of particle i, and check whether the dimensions of position u_i are out of bounds, if it is out of bounds, then take the upper bound, if it is out of bounds, then take the lower bound; Calculate the fitness f (u_i) of particle i, i ∈ [1,m], f (u) is the fitness function.

Step 5: If the fitness f (u_i) of particle i is better than the fitness f (P_{best}) of the individual's own extreme value P_{best}, replace P_{best} with the particle's current position u_i; if the fitness f (u_i) of particle i is better than the fitness f (G_{best}) of the global extreme value G_{best} in the current iteration, the global extreme value G_{best} is replaced with the current position of the particle u_i.

Step 6: If the number of running iterations reaches the preset maximum value of the particle swarm algorithm, the algorithm stops and outputs the global optimal solution G_{best} and the corresponding global optimal value f (G_{best}).

Step 7: Inverse map the global optimal particle position vector G_{best} obtained from the whole particle swarm to the neural network, solve and update the neural network connection weights and thresholds, and repeat the training and learning of the sample data set.

Step 8: Test the trained network with the normalized test sample dataset, output the inverted normalized test result value, and round its output result, the algorithm ends.

The flowchart of the particle swarm BP neural network decoupling algorithm is shown in Figure 10.

VI. CALIBRATION TESTS AND ERROR ANALYSIS

A. STATIC CALIBRATION TEST

This paper uses a self-made pulley calibration device for static calibration, which can accurately apply the calibration force/torque in all directions, is simple to operate and has a stable force value. In the experiment, the loading method adopts the pulley pulling force method, and the weights used are of M1 grade accuracy. The calibration apparatus is depicted in Figure. 11, in which weight 1 produces the calibration force in the negative direction of the X-axis, weight 2 produces the calibration force in the positive direction of the Z-axis, and weight 3 produces the calibration moment in the negative direction of the YM, and the other directions of the force/torque are generated in a similar way. The calibration device can generate force/torque in multiple directions at the same time, which facilitates testing and experimentation of combined force/torque.

Using the self-made calibration test tooling will be applied to the system in a certain direction 5KG, 10KG, 15KG, 20KG, 25KG, 30KG, 35KG, 40KG force, force arm length of 10 cm, under the same torque to take the average value of 100 times, Table 1 is the x-axis direction of the different sizes of the force applied to the direction of the torque z-axis produced by the small voltage signals. Table 2 is the tiny voltage signal in Table 1 after the amplification circuit amplified voltage signal.

As can be seen from Tables 2 and Table 3, at the same time, the voltage output values of the other four directions also change, especially the voltage output value of the Mz direction has a larger change, which means that the force applied in the X direction also has an effect on the measurement of the other four directions.

From Figure 12 and Figure 13, it can be seen that with the increase of loaded weight, Fx, Mz is roughly linear change, and the signal amplified by the signal amplification module, the trend of each signal change is the same.

It can be seen that the sensitivity of the acquisition module can reach 4mV/V, and the signal amplification module has strong stability. Inter-dimensional coupling is a major factor affecting the measurement precision of multidimensional force/torque sensors, and the advantages and disadvantages of the decoupling algorithms have a direct influence on the precision of the sensors.

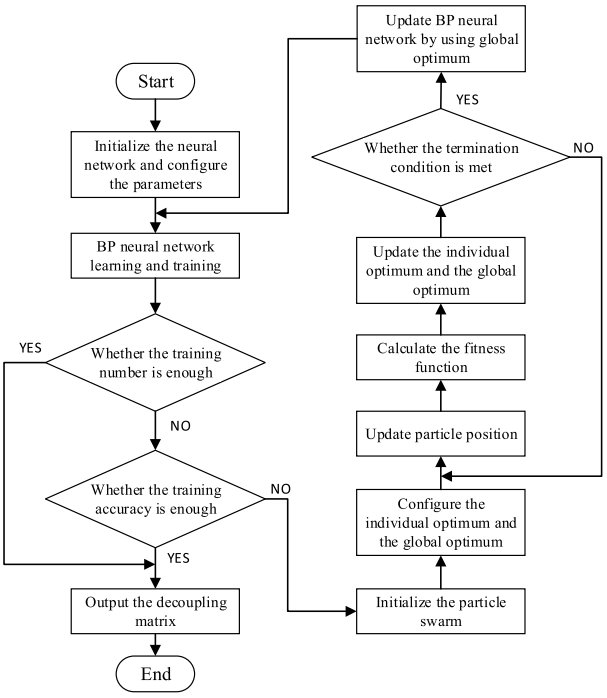

FIGURE 10. Flow chart of decoupling algorithm of particle swarm BP neural network.

TABLE 2. Data obtained by applying force along the X-axis (mV).

Group	F_x	F_y	F_z	M_x	M_y	M_z
1	10.28	9.64	10.16	10.36	9.76	9.64
2	11.12	9.72	10.12	10.24	9.96	10.52
3	11.92	9.64	10.28	9.88	10.04	11.36
4	12.64	9.52	10.44	9.80	10.16	12.16
5	13.60	9.60	10.40	9.84	10.36	13.24
6	14.36	9.68	10.60	9.68	10.56	14.00
7	15.40	9.88	10.68	9.56	10.68	15.08
8	16.20	9.80	10.84	9.6	10.84	16.04
9	17.04	9.76	10.96	9.44	11.00	17.08

TABLE 3. Data obtained by applying force along the X-axis (V).

Group	F_x	F_y	F_z	M_x	M_y	M_z
1	2.56	2.40	2.52	2.58	2.43	2.40
2	2.78	2.42	2.53	2.55	2.48	2.65
3	2.98	2.40	2.56	2.47	2.52	2.82
4	3.19	2.39	2.61	2.44	2.57	3.07
5	3.39	2.41	2.60	2.42	2.58	3.33
6	3.62	2.43	2.62	2.41	2.64	3.54
7	3.88	2.45	2.66	2.35	2.68	3.78
8	4.07	2.41	2.72	2.40	2.72	4.00
9	4.25	2.46	2.75	2.32	2.77	4.23

B. DECOUPLING OF MEASUREMENT DATA

The collected data is transferred to the upper computer display panel via RS-422 communication module, which can convert the voltage signal value to the quality measurement

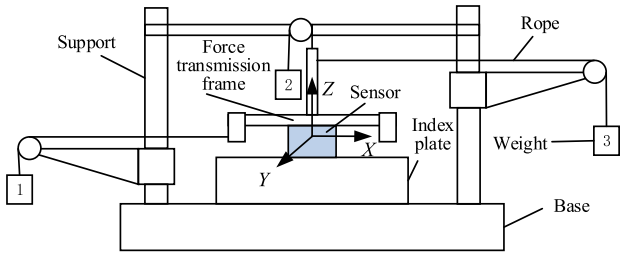

FIGURE 11. Calibration device diagram.

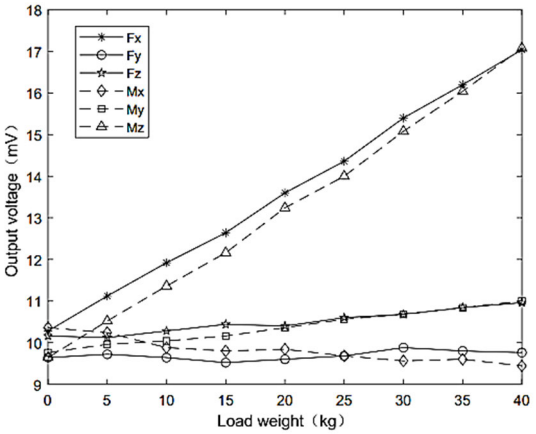

FIGURE 12. Line chart of voltage values applied along the X axis.

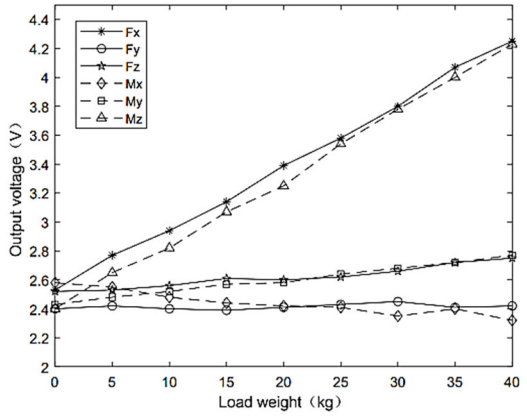

FIGURE 13. Line chart of the amplified voltage of the original signal.

value. Table 4 presents a comparison between the recorded data and the initial data.

Since the test data is the force in the Fx direction and the torque in the Mz direction, the crosstalk values in the Fy, Fz, Mx and My directions are obtained by calculation, and Table 5 shows the crosstalk value data in these four directions.

As can be seen from Table 5, only the crosstalk value in Fy direction is lower than 5%, and the crosstalk value in other directions is greater than 10%. In this case, the inter-dimensional crosstalk will seriously affect the accuracy of the sensor. In this case, inter-dimensional coupling emerges as the primary error source for the 6a-sensors.

TABLE 4. Comparison between measured data and original data.

Group	Data type	F_x	F_y	F_z	M_x	M_y	M_z
1	calibration value	5.000	0.000	0.000	0.000	0.000	0.500
	measured value	5.091	0.462	0.231	0.071	0.115	0.557
2	calibration value	10.000	0.000	0.000	0.000	0.000	1.000
	measured value	9.715	0.006	0.938	0.153	0.205	0.935
3	calibration value	15.000	0.000	0.000	0.000	0.000	1.500
	measured value	14.572	0.238	2.096	0.226	0.317	1.486
4	calibration value	20.000	0.000	0.000	0.000	0.000	2.000
	measured value	19.193	0.234	1.869	0.276	0.331	1.989
5	calibration value	25.000	0.000	0.000	0.000	0.000	2.500
	measured value	24.517	0.692	2.335	0.291	0.365	2.521
6	calibration value	30.000	0.000	0.000	0.000	0.000	3.000
	measured value	30.525	1.154	3.268	- 0.368	0.398	3.056

TABLE 5. Crosstalk value of F_y, F_z, M_x and M_y direction.

Group	Direction	Crosstalk value
1	F_y	3.64%
2	F_z	10.85%
3	M_x	10.05%
4	M_y	11.70%

1) DATA PREPROCESSING

Dimensional crosstalk will seriously affect the accuracy of the sensor. In this case, inter-dimensional coupling emerges as the primary error source for the 6a-sensors. Statistical measurement method and the average value of the method, according to the principle of the 3 - σ statistics to remove the gross error in the measured data obtained from the effective measurement of the average value of the smoothing! In practice, the sampling of one hundred groups as a processing unit, respectively, after processing, because the group is now more in the x direction, loaded with 15kg load, respectively, in different directions, loaded with different (y15kg, z15kg), such as the case shown in Table 6, the data for the mean square error.

2) FEATURE SUPPLEMENT

After collecting data, in order to increase the model's ability to learn the features, cross features and one-heat encoding are introduced as auxiliary features, where cross features are the

TABLE 6. Comparison table before and after introduction of the method.

No.	main direction	Sub-directional	pre-introduction	post-institutional
1		Mx	2.352	1.252
2	Fx	My	2.421	1.728
3		Mz	2.385	1.529
4		Mx	2.444	1.433
5	Fy	My	2.397	1.761
6		Mz	2.321	1.239
7		Mx	2.304	1.357
8	Fz	My	2.336	1.394
9		Mz	2.479	1.257

Loading force 150N, torque 1.5N-M

TABLE 7. The decoupling error comparison before and after feature supplement.

Group	Type	F_x	F_y	F_z	M_x	M_y	M_z
1	Without feature supplement	2.26 %	2.965 %	2.72 %	2.92 %	2.25 %	2.845 %
2	With feature supplement	1.226 %	1.786 %	1.786 %	1.024 %	0.985 %	1.125 %

difference between the collected voltage in each direction and the zero-point voltage taken as a do-over. The one-heat encoding is: if a force is applied or a force torsion is generated in a certain direction, the acquisition feature along that direction is 1, otherwise it is 0.

Under the premise of ensuring the same training set and model structure, the decoupling situation before and after the introduction of feature supplementation is compared, and the calculation method of Type II error is used for calculation, and the calculation results are detailed in Table 7.

In summary after the introduction of feature supplementation, the coupling error is improved by about 1%.

3) DATA DECOUPLING

This algorithm module uses neural network algorithm for modeling, to establish a regression model based on deep learning neural network, the data collected by the sensors for collection, pre-processing, labeling, and sent to the model for learning, training to obtain, based on the loss function of the mean squared error (MSE) is less than 0.05, which calculates the average of the squares of the difference between the predicted value and the true value of the metrics are expressed as in(10), the smaller the mean square error, the less disparity exists between the model's prediction and the actual value.

$$MSE = \frac{1}{n}\sum \left(y_{pred} - y_{ture}\right)^2 \tag{10}$$

TABLE 8. Comparison between fitted data and original calibration data.

Group	Data type	F_x/kg	F_y/kg	F_z/kg	M_x / N · M	M_y / N · M	M_z / N · M
1	calibration value	0.00	0.00	0.00	0.00	0.00	0.00
	fitted value	0.02	0.03	0.00	0.00	0.00	0.00
2	calibration value	5.00	5.00	5.00	0.50	0.50	0.50
	fitted value	5.03	5.04	5.01	0.49	0.49	0.49
3	calibration value	10.0	10.0	10.0	1.00	1.00	1.00
	fitted value	9.98	9.95	10.0	0.99	0.99	1.00
4	calibration value	15.0	15.0	15.0	1.50	1.50	1.50
	fitted value	14.9	15.0	15.0	1.50	1.49	1.49
5	calibration value	20.0	20.0	20.0	2.00	2.00	2.00
	fitted value	19.9	20.0	20.0	2.00	2.00	2.00
6	calibration value	25.0	25.0	25.0	2.50	2.50	2.50
	fitted value	24.9	24.9	25.0	2.49	2.50	2.49
7	calibration value	30.0	30.0	30.0	3.00	3.00	3.00
	fitted value	29.9	30.0	29.9	3.00	3.00	3.00

Cross-validation is used in the data validation scheme, and the cross-validation scheme adopts K-fold cross-validation, in which K takes the value of 5, i.e., 80% of the data in the dataset is used for model training, and the remaining 20% is used for cross-validation, which can comprehensively assess the performance of the model and reduce the chance introduced due to the division of data.

After training the model, the data is taken for validation, in order to ensure the generalizability of the model, 8 sets of parameters that are not fed into the model for training are taken for error validation, and the error is calculated with reference to (11) to get the table of calculated errors as shown in Table 8.

$$\mathrm{E} = \frac{\left|M_{real} - M_{fit}\right|}{M_{F.s}} \tag{11}$$

It can be calculated that the algorithm module, in the fitting process, the maximum error of fitting the force sum is 0.167% and the maximum error of fitting the torque is 0.153%.

C. ANALYSIS OF DECOUPLING EFFECT

The 6a-sensors is a sensor that measures the value of force/torque, and in order to evaluate the degree of decoupling of a sensor, there needs to be an accuracy index of the sensor's

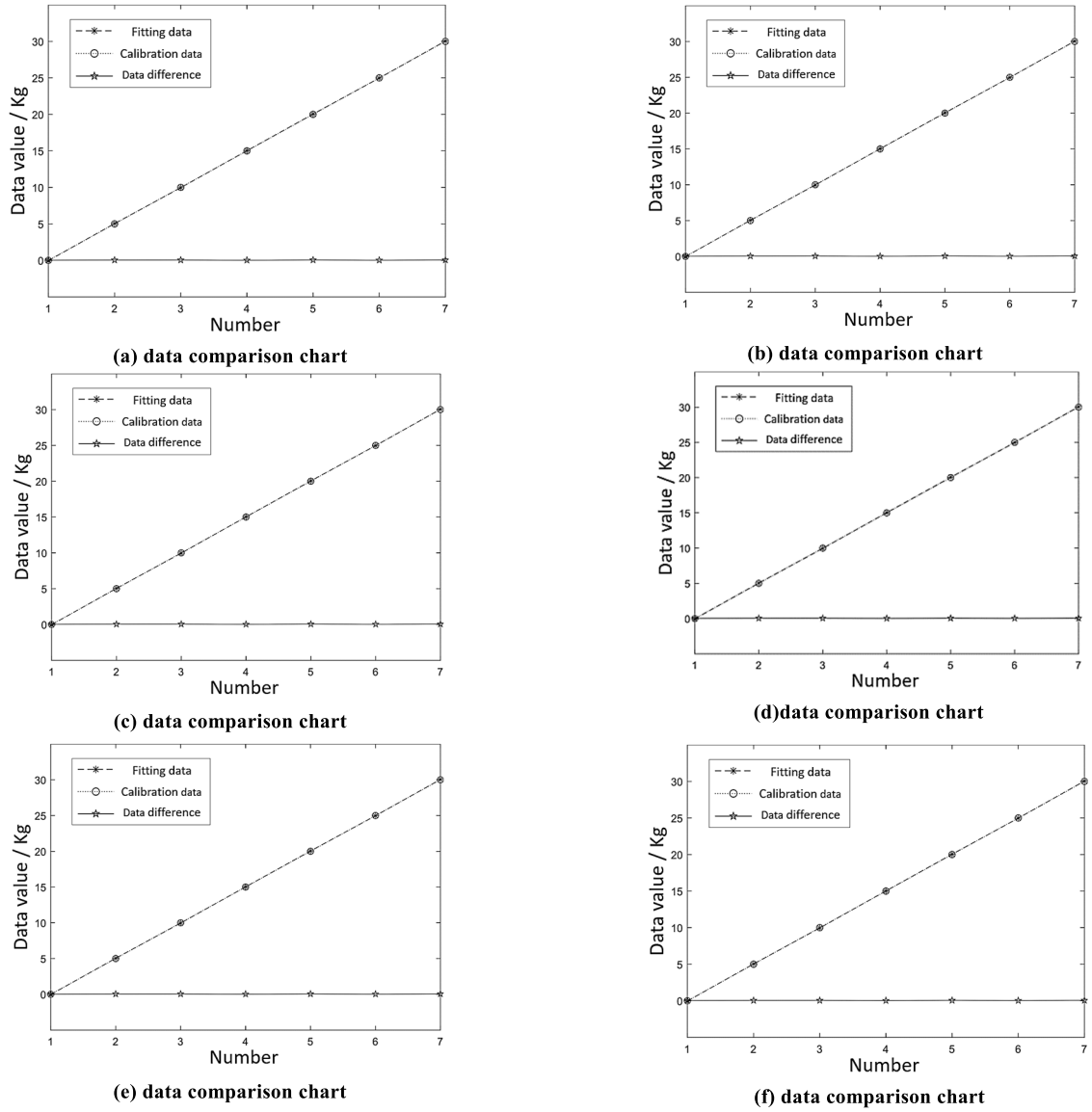

FIGURE 14. Comparison between fitted data and original calibration data.

measured value. We use the coupling error as follows.

$$Couplingerror = \sqrt{\frac{\sum |y_{ij}|}{|y_i|}} (i \neq j) \tag{12}$$

where y_i denotes the full scale value of the force (or torque) that can be applied in the i direction, and y_{ij} denotes the maximum force (or torque) value measured in the i direction when a force (or torque) value is applied in the j direction and no force (or torque) is applied in the other five directions. The comparison of the accuracy when the sensor is uncoupled and after matrix decoupling and DL decoupling is shown in Table 9.

From Table 9, we know that compared with the pre-decoupling, the matrix decoupling coupling error has about 5% improvement; compared with the matrix decoupling, the DL decoupling coupling error has about 2% improvement. Therefore, decoupling based on neural network algorithm significantly improves the accuracy of the sensor.

TABLE 9. Precision comparison of the sensor without decoupling and after matrix decoupling and DL decoupling.

Method	F_x	F_y	F_z	M_x	M_y	M_z
None	7.759 %	8.735 %	8.186 %	5.258 %	5.698 %	6.025 %
matrix	4.365 %	2.965 %	3.720 %	2.920 %	1.725 %	1.845 %
polynomial	2.231 %	3.054 %	3.172 %	2.101 %	6.214 %	3.271 %
DL	1.226 %	1.786 %	1.786 %	1.024 %	0.985 %	1.125 %

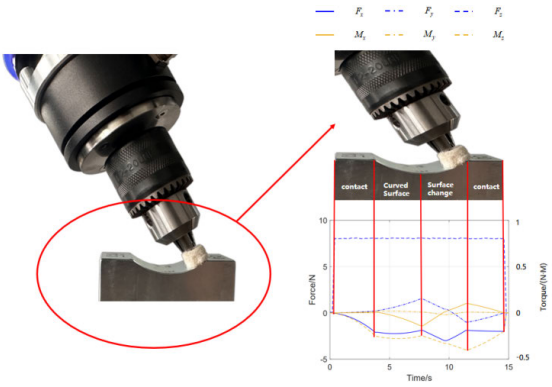

FIGURE 15. Application of 6a-sensors in grinding manipulator.

TABLE 10. Comparison between 6a-sensors based on DL algorithm and other 6a-sensorss.

Sensor type	Based on DL algorithm	Eight beam spoke type	PSO-FLANN	Static decoupling algorithm
sensitivity	0.01%	0.03%	0.01%	0.01%
accuracy	1.18%	2.6%	1.89%	2.28%
crosstalk	0.2%	0.5%	0.42%	0.32%

D. ACCURACY AND ERROR ANALYSIS

The comprehensive evaluation of a sensor should be based on its sensitivity, accuracy, crosstalk and other aspects. Table 10 shows the data comparison between the six-dimensional force sensor based on the DL algorithm in the paper and the six-dimensional force sensor commonly used in scientific research.

As can be seen from Table 10, the performance of common 6a-sensors in the scientific research field is basically the same in terms of sensitivity, and in terms of accuracy, among the other sensors in the scientific research field mentioned above, PSO-FLANN 6a-sensors has the highest accuracy, and there is an improvement of 0.71% in the 6a-sensors based on the DL algorithm, and in terms of the degree of crosstalk, static decoupling algorithm 6a-sensors has the lowest degree of crosstalk, and 6a-sensors based on the DL algorithm has the lowest degree of crosstalk, and 6a-sensors based on the DL algorithm has a 0.12% improvement. In summary, the six-axis force based on the DL algorithm achieves the characteristics of high sensitivity, high accuracy and low crosstalk, and the comprehensive performance is significantly improved.

VII. CASE APPLICATION EXPERIMENTS

To further test the usability of the 6a-sensors, in this paper the 6a-sensors was used in a sanding robot arm to measure the interaction force between the sanding head and a workpiece with a non-regular surface (Figure 15).

For the workpiece shown in Figure 15, the normal contact force between the sanding head and the surface of the workpiece was determined manually to be 8 N and kept constant in order to ensure the sanding effect and its consistency. The above mentioned 6a-sensors is mounted to the sanding robot arm to measure the interaction force between the sanding head and the workpiece and to realize the force feedback control of the robot arm. When the sanding head comes into contact with the surface of the workpiece, the normal contact force increases rapidly to the maximum setting (8 N). After the robot arm starts tracking the surface, the 6a-sensors measures the slight change in normal force and feeds back to the robot arm control system, allowing the robot arm to autonomously adjust to achieve constant normal force tracking.

The actual test results show that the 6a-sensors accurately measures both the three-dimensional contact force and torque during the polishing process when the grinding head interacts with the surface of the workpiece, and feeds back to the control system well to ensure that the mechanical polishing work achieves good results. This application provides important data for further evaluation of mechanical polishing operations and confirms the performance and usability of the sensor.

VIII. CONCLUSION

In this design, for the three major difficulties of 6a-sensors weak signal sensing difficulty, weak signal amplification and acquisition difficulty and six-axis force data decoupling difficulty, the innovative design based on the crossbeam structural elastomer, the innovative design based on the programmable multiplexed weak signal acquisition system, and the six-axis force decoupling algorithm based on the deep learning are respectively put forward. Through the homemade six-axis force test calibration tooling for the designed work of sensitivity, accuracy and crosstalk test, the test results and literature [1], [2], [3] corresponding indicators were compared, sensitivity indicators and other three literature data are basically the same, accuracy and crosstalk of the two indicators have a more obvious improvement. The experimental results show the effectiveness of the method proposed and realized in this design. At the same time, the results achieved in this design lay a solid foundation for the subsequent in-depth study of 6a-sensorss.

Although the 6a sensor designed in this paper has made great progress in the elastomer structure design, data method and acquisition card design, data decoupling algorithm design. However, there are still the following limitations, the decoupling algorithm should be adjusted according to the different structure and different materials of the elastomer to be entered through the measured data; the elastomer application process, due to the working environment and the elastomer itself need to repeat the calibration; the method is only applicable to static labelling, for the dynamic situation is not applicable for the time being. Through the practice of this design, we have accumulated a lot of experience in the research and development of 6a sensors and found a lot of problems that need to be further improved, and at the same time, we are more clear about the direction of the next step of efforts, and we will explore the dynamic characteristics and

propose the method of dynamic labelling in the subsequent work. And we will add the acceleration sensing in each direction in the follow-up work, and explore the decoupling and calibration method of 12-dimensional force sensor, which is a very meaningful learning.

REFERENCES

[1] J. Bai and Y. Xu, "Research on the development of manufacturing industry from the perspective of industrial robot," *Mech. Eng. Autom.*, vol. 6, pp. 223–224, 2020.
[2] U. Kim, D.-H. Lee, Y. B. Kim, D.-Y. Seok, and H. R. Choi, "A novel 6a-sensors for robotic applications," *IEEE/ASME Trans. Mechatron.*, vol. 22, no. 3, pp. 1381–1391, Jun. 2017.
[3] L. Fu and A. Song, "Dynamic characteristics analysis of the 6a-sensors," *J. Sensors*, vol. 2018, pp. 1–11, Dec. 2018.
[4] Y.-J. Li, G.-C. Wang, X. Yang, H. Zhang, B.-B. Han, and Y.-L. Zhang, "Research on static decoupling algorithm for piezoelectric six axis force/torque sensor based on LSSVR fusion algorithm," *Mech. Syst. Signal Process.*, vol. 110, pp. 509–520, Sep. 2018.
[5] M. Y. Cao, S. Laws, and F. R. Y. Baena, "Six-axis force/torque sensors for robotics applications: A review," *IEEE Sensors J.*, vol. 21, no. 24, pp. 27238–27251, Dec. 2021.
[6] L. Fu and A. Song, "A polyetheretherketone 6a-sensors," *IEEE Access*, vol. 7, pp. 105391–105401, 2019.
[7] H. B. Yan, W. Cao, and N. N. Sun, "Inverse kinematics analysis and time-minimum motion planning of a photovoltaic array cleaning robotic arm based on BP neural network," *ACTA Energiae Solaris Sinica*, vol. 43, no. 10, pp. 43–51, 2022, doi: 10.19912/j.0254-0096.tynxb.2021-0427.
[8] C. Li and C. Zhang, "Analysis of the structure for the 6a-sensors," *Observ. Control Technol.*, vol. 39, no. 5, pp. 41–48, 2020.
[9] Z. Wang and J. Yao, "Statically determinate measurement model and calibration method of statically indeterminate 6a-sensors," *Yi Qi Yi Biao Xue Bao/Chin. J. Scie. Instrum.*, vol. 34, no. 9, pp. 1927–1933, 2013.
[10] W. Niu, R. Huang, and J. Han, "Signal acquisition system of micro sensor based on FPGA," *Sensors Microsyst.*, vol. 38, no. 5, pp. 104–106, 2019.
[11] Y. Liu, G. P. Li, and G. K. Zuo, "Design of force sensor signal acquisition and processing system based on STM32," *Sensors Microsyst.*, vol. 36, no. 7, pp. 112–115, 2017.
[12] Z. Wang, X. Zhang, and M. Li, "Stiffness analysis and parameter optimization of six-dimensional force sensor with the novel circular flexible spherical joint," *Meas. Sci. Technol.*, vol. 35, no. 1, Jan. 2024, Art. no. 015114.
[13] M.-T. Ha and C.-G. Kang, "A user-friendly and economical six-axis force/torque sensor with wireless communication for force control and monitoring," *IEEE Sensors J.*, vol. 23, no. 3, pp. 1952–1961, Feb. 2023.
[14] G. A. Kebede, A. R. Ahmad, S.-C. Lee, and C.-Y. Lin, "Decoupled six-axis force–moment sensor with a novel strain gauge arrangement and error reduction techniques," *Sensors*, vol. 19, no. 13, p. 3012, Jul. 2019.
[15] F. J. A. Chavez, S. Traversaro, and D. Pucci, "Six-axis force torque sensor model-based in situ calibration method and its impact in floating-based robot dynamic performance," *Sensors*, vol. 19, no. 24, p. 5521, Dec. 2019.
[16] C. Chen, "Research on calibration technique of 6a-sensors," Zhejiang Sci-Tech Univ., Hangzhou, China, Tech. Rep., 2022.
[17] X. Wu, A. Song, and Z. Wang, "The study of static decoupling algorithm for 6a-sensors and static calibration," *J. Sens. Technol.*, vol. 26, no. 6, pp. 851–856, 2013.
[18] W. Xiao and W. Dong, "Research on nonlinear static decoupling of 6a-sensors," *J. Navigat. Eng. Univ.*, vol. 24, no. 3, pp. 46–51, 2012.
[19] G. Wang, X. Yi, and L. Wang, "Several problems in the development of 6a-sensors," *Robots*, vol. 11, no. 2, pp. 474–478, 1997.
[20] C. Mao, A. Song, and X. Gao, "Research and application of static decoupling algorithm for 6a-sensors," *Sensor Technol.*, vol. 28, no. 2, pp. 205–210, 2015.
[21] L. Jiang, H. Liu, and H. Cai, "Neural network-based static decoupling of multidimensional force sensors," *China Mech. Eng.*, vol. 13, no. 24, pp. 2100–2103, 2002.
[22] X. Wang and H. Sun, "Fault diagnosis of cascaded inverter based on PSO and neural network," *Comput. Simul.*, vol. 32, no. 7, pp. 421–425, 2015.
[23] Z. J. Wang, X. T. Zhang, and M. X. Li, "Research on decoupling algorithm of six-dimensional force sensor based on polynomial fitting," *Chin. J. Eng. Design*, vol. 30, no. 5, p. 6, 2023, doi: 10.3785/j.issn.1006-754X.2023.00.063.

WEIZHENG REN was born in October 1974. He received the Ph.D. degree in electrical engineering from Beijing University of Posts and Telecommunications, Beijing, China, in July 2011. He is currently the Director of the Experimental Center, School of Modern Post, Beijing University of Posts and Telecommunications. His main research interests include the IoT, educational robots, and artificial intelligence.

KAILE YU is currently pursuing the Ph.D. degree in electronic engineering with Beijing University of Posts and Telecommunications (BUPT), Beijing, China. His research interests include electronic system designs, multi-dimensional force sensors, and mechanical system control.

YIRAN ZHANG is currently pursuing the M.S. degree with the School of Electronic Engineering, Beijing University of Posts and Telecommunications, Beijing. His research interests include force sensors and force control.

YUTONG GE is currently pursuing the M.S. degree in electronic science and technology with Beijing University of Posts and Telecommunications, Beijing, China. His research interests include robot control, sensors, and artificial intelligence.

YUXIAO LI is currently pursuing the M.S. degree with the School of Electronic Engineering, Beijing University of Posts and Telecommunications, Beijing, China, with a focus on six-axis force sensors.